The accepted version:

Liang, S., Cheng, C., Jia, K., Jiang, B., Liu, Q., Xiao, Z., Yao, Y., Yuan, W., Zhang, X., Zhao, X., & Zhou, J. (2020). The Global LAnd Surface Satellite (GLASS) products suite. B*ulletin of the American Meteorological Society*, DOI: 10.1175/BAMS-D-1118-0341.1171

The Global LAnd Surface Satellite (GLASS) product suite

Shunlin Liang[a], Jie Cheng[b,c,*], Kun Jia[b,c*], Bo Jiang[b,c,*], Qiang Liu[b,d,*], Zhiqiang Xiao[b,c,*], Yunjun Yao[b,c,*], Wenping Yuan[e,*], Xiaotong Zhang[b,c,*], Xiang Zhao[b,c,*], Ji Zhou[f,*]

[a]Department of Geographical Sciences, University of Maryland, College Park, MD 20742, USA

[b]State Key Laboratory of Remote Sensing Science and Beijing Engineering Research Center for Global Land Remote Sensing Products, Beijing Normal University, Beijing 10075, China

[c]Institute of Remote Sensing Science and Engineering, Faculty of Geographical Sciences, Beijing Normal University, Beijing, China

[d]College of Global Change and Earth System Science, Beijing Normal University, Beijing, China

[e]School of Atmospheric Sciences, Sun Yat-sen University, Guangzhou 510245, Guangdong, China

[f]School of Resources and Environment, Center for Information Geoscience, University of Electronic Science and Technology of China, Chengdu 611-731, China

*joint 2nd co-authors, equally contributed to this paper

Corresponding author address: Department of Geographical Sciences, University of Maryland, College Park, MD 20742, USA. Email: sliang@umd.edu

Capsule: Overview of the 12 Global LAnd Surface Satellite (GLASS) products that encompass surface radiation and vegetation variables with long-term time series (from 1981 or 2000 to the present), high resolutions (500 m, 1 km and 0.05°), and high qualities and accuracies

Abstract

The Global LAnd Surface Satellite (GLASS) product suite currently contains 12 products, including leaf area index, fraction of absorbed photosynthetically active radiation, fraction of green vegetation coverage, gross primary production, broadband albedo, broadband longwave emissivity, downward shortwave radiation and photosynthetically active radiation, land surface temperature, downward and upwelling thermal radiation, all-wave net radiation, and evapotranspiration. These products are generated from the Advanced Very-High-Resolution Radiometer and Moderate Resolution Imaging Spectroradiometer satellite data. Their unique features include long-term temporal coverage (many from 1981 to the present), high spatial resolutions of the surface radiation products (1 km and 0.05°), spatial continuities without missing pixels, and high quality and accuracy based on extensive validation using in situ measurements and inter-comparisons with other existing satellite products. Moreover, the GLASS products are based on robust algorithms that have been published in peer-reviewed literature. Herein, we provide an overview of the algorithm development, product characteristics, and some preliminary applications of these products. We also describe the next steps, such as improving the existing GLASS products, generating more climate data records (CDRs),

broadening product dissemination, and fostering their wider utilization. The GLASS products are freely available to the public.

1. Introduction

The world is currently confronted with historically unprecedented environmental challenges, particularly those related to climate change. To better understand, monitor, and predict those changes, researchers need access to high-quality satellite products of different bio- and geo-physical variables. Though several international space agencies produce high-level land products from different satellite observations, a major limitation of these products is their short temporal coverages, due to the fact that they are usually generated from observations made by a specific satellite sensor that has a limited life span. The remote sensing community has started to use the satellite data to generate climate data records (CDRs) of the essential climate variables (ECVs) defined by the Global Climate Observing System (GCOS 2016), where CDRs are defined as time series of measurements with sufficient length, consistency, and continuity to determine climate variability and changes (NRC 2004). However, not many land CDRs are currently available to the public, and more efforts to produce these land CDRs are critically needed.

Production of the Global LAnd Surface Satellite (GLASS) product suite began in 2009 with five initial products (Liang et al. 2013a; Liang et al. 2013b), and continued development has led to more than a dozen products with improved accuracies and qualities over previous versions of the same products as well as other comparable products. Currently, 12 of these products are officially released. The GLASS products are primarily based on NASA's Advanced Very-High-Resolution Radiometer (AVHRR) long-term data record (LTDR) (https://ltdr.modaps.eosdis.nasa.gov) and Moderate Resolution Imaging

Spectroradiometer (MODIS) data, in conjunction with other satellite data and ancillary information.

The characteristics of the 12 GLASS products (version 4), several of which correspond to ECVs, are outlined in Table 1. Compared to other existing satellite products, the GLASS products have several unique features: 1) the new products are not available from other sources (e.g., longwave broadband emissivity from both AVHRR and MODIS; downward longwave radiation from MODIS); 2) long-term time series data (many products span from 1981 to the present); 3) high spatial resolutions of the surface radiation products (1 km or 0.05°), which are much finer than other commonly used products (≥ 100 km), such as the gridded Clouds and the Earth's Radiant Energy System (CERES) products (1°) and the Global Energy and Water Exchanges (GEWEX) surface radiation budget (SRB) products (280 km); 4) spatial continuities with no data gaps; and 5) higher accuracies and temporal consistencies based on direct validation using in situ measurements and product inter-comparisons.

Algorithm development is critical for generating satellite products. The algorithms for the current version of the GLASS products are provided in each of the following sections, and additional details regarding comparisons with other algorithms can be found in a recent book (Liang and Wang 2019).

The GLASS products have recently been used for different applications . To facilitate more extensive utilization of these products by the broader community, this paper provides an overview of the GLASS products' characteristics, inversion algorithms, validation results and some preliminary applications. On-going activities focused on expanding and enhancing the GLASS products are also described.

2. Algorithm development, Product characteristics, and Applications

2.1 Leaf area index (LAI)

Conceptually, there are both true LAI and effective LAI. True LAI is defined as half of the total green leaf area per unit of horizontal ground surface area, while the effective LAI is the true LAI multiplied by the clumping index that quantifies the level of foliage grouping within distinct canopy structures relative to a random distribution (He et al. 2012). True LAI has been widely used by most models (Myneni et al., 2002).

The GLASS LAI product represents the true LAI that is generated using general regression neural networks (GRNNs) that are trained using the integrated satellite LAI time-series and the MODIS surface reflectance data (Xiao et al. 2014) or the AVHRR surface reflectance data (Xiao et al. 2016c). The LAI time series integrates the MODIS (Myneni et al. 2002) and the Carbon cYcle and Change in Land Observational Products from an Ensemble of Satellites (CYCLOPES) (Baret et al. 2007) LAI products. Unlike existing neural network methods that use only satellite data acquired at a specific time to retrieve the LAI, the GLASS LAI algorithm uses pre-processed reflectance data from an entire year to train the GRNNs and to estimate the one year LAI profile for each pixel since it is

advantageous to use a surface reflectance time series rather than an individual reflectance value. Furthermore, the surface reflectance data from atmospheric correction is frequently contaminated by clouds, so pre-processing the surface reflectance data is an essential step in eliminating the impacts of this “noise”. Different algorithms have been developed to generate temporally continuous and smoothed surface reflectance time series (Tang et al. 2013; Xiao et al. 2015a; Xiao et al. 2017b). Our experiences reveal that effective pre-processing techniques need to be employed to produce a high-quality LAI product.

Compared to other long-term LAI products, the GLASS LAI product has been shown to have higher quality and accuracy (Xiao et al. 2017a). Independent direct validation has also demonstrated that the GLASS LAI product exhibits the best accuracy, with R^2 = 0.70 and root-mean-square error (RMSE) = 0.96 globally and R^2 = 0.94 and RMSE = 0.61 over China (Li et al. 2018b). Another independent validation study also showed that the GLASS LAI product has the lowest uncertainty, followed by GEOV1 (the first version of Geoland2 satellite products) and MODIS for all the biome types tested (Xu et al. 2018). The high quality of the GLASS LAI product is characterized by its spatial and temporal continunity (no gaps or missing values), temporal stability, and representation of vegetation phenology.

Additionally the GLASS LAI products have been utilized to estimate other variables from satellite data, such as calculating the fraction of absorbed photosynthetically active

radiation (FAPAR) (Xiao et al. 2016b; Xiao et al. 2015b), fraction of vegetation coverage (Xiao et al. 2016a), broadband emissivity (BBE) over vegetated surfaces (Cheng et al. 2016; Meng et al. 2017), gross primary production (GPP) (Liu et al. 2018; Liu et al. 2015; Tian et al. 2017) and evapotranspiration (ET) (Sun et al. 2016; Tian et al. 2015), mapping wall-to-wall vegetation height in China (Huang et al. 2017), generating regional phenology (Wang et al. 2017c), detecting forest disturbances (Wang et al. 2017a), and characterizing the ecosystem dynamics within a watershed that has complex topography (Liu et al. 2017). A recently developed remote sensing data assimilation framework has also used the GLASS LAI product to simultaneously estimate a group of atmospheric and land surface parameters (Ma et al. 2017a; Ma et al. 2017b; Ma et al. 2018; Shi et al. 2016; Shi et al. 2017; Xiao et al. 2015c).

The GLASS LAI products have also been used to drive various process-oriented models, such as the Lund-Potsdam-Jena dynamic global vegetation model (LPJ-DGVM), to achieve a better agreement between the estimated and observed GPP (Ma et al. 2017c). A hydrological model used to determine the hydrological responses to reforestation has also utilized these LAI products (Liu et al. 2016).

The LAI products have also been used to evaluate land surface models (Bao et al. 2014; Druel et al. 2017; Guimberteau et al. 2018; Tesemma et al. 2015) and Earth system models (Huang et al. 2016), investigate vegetation-atmosphere interactions in order to evaluate the response of vegetation to the changing environment (Jiapaer et al. 2015), detect greening trends at different spatial scales (Li et al. 2018a; Piao et al. 2015; Zhu et

al. 2016b), among others (Wang et al. 2018; Yu et al. 2018). The LAI products have also been assimilated into land surface models (Zhao et al. 2016).

2.2 Fraction of Absorbed Photosynthetically Active Radiation (FAPAR)

FAPAR is a key biophysical variable that is directly related to the photosynthetic activity of plants, and is an indicator of the presence and productivity of living vegetation, as well as the intensity of the terrestrial carbon sink.

Instead of estimating the FAPAR directly from satellite data, the GLASS FAPAR products are derived from the GLASS LAI products and other auxiliary information (Xiao et al. 2015b). This method calculates the FAPAR values based mainly on the photosynthetically active radiation (PAR) transmittance of the entire canopy. An advantage of this approach is to ensure physical consistency between the LAI and FAPAR products. The GLASS FAPAR products represent the values at 10:30 AM local time, which are close approximations of daily average FAPAR (Fensholt et al. 2004).

The long-term GLASS FAPAR product from the AVHRR was compared with two similar products: the National Centers for Environmental Information (NCEI) and the third-generation Global Inventory Monitoring and Modeling System (GIMMS3g) AVHRR FAPAR products. The GLASS product exhibits better quality and accuracy (Xiao et al. 2018).

The GLASS FAPAR products have been used in many studies. For example, Zhu et al. (2016a) and Wang et al. (2017b) demonstrated that substantial improvements in estimating the tower GPP were achieved by substituting the GLASS FAPAR product for

the MODIS FAPAR product, especially for croplands. Hu et al. (2018) also incorporated the GLASS FAPAR product into their GPP calculations.

2.3 Fractional vegetation cover (FVC)

FVC generally refers to the fraction of green vegetation as seen from the nadir of the total statistical area. FVC is an important parameter for describing land surface vegetation conditions required by many land surface models, weather prediction models, regional and global climate models, hydrological models and global change studies.

Multiple global FVC products have been generated from different satellite datasets; however, many require improvements in accuracy. For example, the GEOV1 FVC product is generally accurate (Camacho et al. 2013), but validation using data from an agricultural region indicates an overestimate of up to 0.2 (Mu et al. 2015).

The GLASS FVC product is based on machine learning methods that use training samples generated from globally distributed high spatial resolution satellite data (Jia et al. 2019). Initially, the GLASS FVC product algorithm for MODIS data was based on the GRNNs method (Jia et al. 2015). After comparing four machine learning methods, including back-propagation neural networks (BPNNs), GRNNs, support vector regression (SVR), and multivariate adaptive regression splines (MARS), the MARS method was chosen to produce the global FVC product from MODIS data. This was due to its high computational efficiency and reasonable accuracy (Yang et al. 2016).

The GLASS AVHRR FVC algorithm was based on the GLASS MODIS FVC product to achieve temporal consistency. First, one year training samples were extracted globally where AVHRR reflectance data and the GLASS MODIS FVC product overlapped. The MARS model was then trained with the training samples and used to estimate the FVC from the pre-processed AVHRR reflectance data. Finally, the estimated FVC from the AVHRR data were linearly corrected based on the GLASS MODIS FVC to obtain the AVHRR FVC consistent with the GLASS MODIS FVC.

The GLASS FVC product has been evaluated by both direct validation and product inter-comparisons (Jia et al. 2019). Based on 44 reference datasets from the VAlidation of Land European Remote sensing Instruments (VALERI) sites with various land cover types, the RMSE of the GLASS FVC from the MODIS data is 0.157, which is comparable to that of the GEOV1 FVC product (RMSE = 0.166). The coefficient of determination (R^2) of the GLASS MODIS FVC is 0.809, which is larger than that of the GEOV1 FVC product (R^2=0.775). The GLASS AVHRR FVC product also has validation results (R^2=0.834, RMSE = 0.145) that are slightly superior to those of the GEOV1 FVC product from AVHRR data (R^2=0.799, RMSE = 0.174). A direct validation of the GLASS FVC product in an agricultural region based on a time series of field FVC measurements indicated that the performance of the GLASS FVC product (R^2=0.86, RMSE = 0.087) was better than the performance of the GEOV1 FVC product (R^2=0.71, RMSE = 0.193) using the same reference data (Jia et al. 2018b). Other validation experiments have been conducted using estimates from high-resolution satellite data and ground measurements (Jia et al. 2018b; Jia et al. 2016).

2.4 Downward shortwave radiation (DSR)

Surface DSR is an essential component of the total energy exchanged between the atmosphere and the surface and is required by most land surface hydrological and ecological models. The earlier GLASS DSR product was based on an improved look-up table (LUT) method using multiple polar-orbiting and geostationary satellite datasets (Zhang et al. 2014). However, it was too time consuming to generate a long-term global DSR product using this method. To overcome this difficulty, the current GLASS DSR product is instead generated from the MODIS top-of-atmosphere (TOA) reflectance based on a direct-estimation method (Zhang et al. 2019).

The GLASS DSR product has a 0.05° spatial resolution and a daily temporal resolution. Validated by ground measurements collected at 525 stations from 2003 - 2015 around the world, the GLASS monthly DSR has an overall bias of 1.24 W m^{-2} and an RMSE of 21.16 W m^{-2}. Moreover, the global land annual mean of the DSR was 184.8 W m^{-2}, with a standard deviation of 0.8 W m^{-2} over a 13-yr (2003–2015) period.

2.5 Downward Photosynthetically Active Radiation (PAR)

PAR is defined as the visible part (400–700nm) of the DSR. It is an essential parameter in ecological modeling that controls the exchange of water vapor and carbon dioxide between vegetation and the atmosphere and is used to estimate global terrestrial vegetation productivity.

Currently, most global radiation products do not have a PAR component, so many users have to calculate PAR by multiplying the DSR by an empirical conversion constant of approximately 0.5 (Liang et al. 2006). The GLASS PAR product was previously produced using the LUT method (Liang et al. 2013b; Zhang et al. 2014). The current version of the PAR product is obtained from the GLASS DSR multiplied by a spatially and temporally variable conversion factor determined from the GEWEX-SRB V3.0 radiative flux products, in which DSR and PAR are provided separately. The accuracy of this method is comparable to that of the previous version of the product. Cai et al. (2014) demonstrated that the GLASS PAR product can produce better estimations of terrestrial GPP over China by comparing it with several other incident radiation products.

2.6 Broadband albedo

Land surface albedo describes the ratio of the upward to downward flux of solar radiation at the surface and is an important indicator of global environmental changes, such as urbanization, deforestation/afforestation, and Arctic sea ice retreat (Dickinson 1983).

Unlike the MODIS albedo products, which are based on inversions of the bidirectional reflectance distribution function (BRDF) model parameters, the GLASS albedo products are based on the direct-estimation method and represent surface albedo under general clear-sky atmospheric conditions. The GLASS albedo algorithm consists of two steps. The first step adopts the direct-estimation algorithm (Qu et al. 2014) to derive the intermediate albedo products, and the second step adopts the spatiotemporal filtering algorithm (Liu et al. 2013a) to generate a smoothed and gap-free product.

The version 3 GLASS albedo product was released in 2012 (Liu et al. 2013b; Peng et al. 2015). The version 4 (V4) GLASS albedo products released in 2019 have been updated with regard to several aspects. In addition to the shortwave (SW) albedo, the products include visible (VIS) and near-infrared (NIR) albedo values. The snow/ice BRDF model has been updated (Qu et al. 2016), and a water surface BRDF model has been adopted for the ocean surface as well as for mixed pixels of water/sea ice (Feng et al. 2016). As a result, the quality and accuracy of the GLASS albedo products over ocean and sea ice areas have been improved (Qu et al. 2016; Feng et al. 2016).

The V4 GLASS shortwave albedo products were validated by tower-based observations from 53 spatially homogeneous global sites (Fig. 1). These measurements are part of the LaThuile Opened dataset from FLUXNET (Baldocchi, et al., 2001). The RMSE was 0.052 for all matched samples. After screening out all the cloudy pixels, the RMSE was reduced to 0.037.

Since it is difficult to obtain ground measurements to directly validate visible and near-IR albedo, we compared these products with the MODIS (C6 MCD43A3) product. They are consistent over snow-free pixels, with RMSE values of 0.018 and 0.022, respectively. However, larger discrepancies were observed over snow/ice pixels, partially due to their differences in spatial resolution.

The GLASS albedo products have been used by many studies. For example, they have been used to calculate surface evapotranspiration (ET) (Carter and Liang 2019), to determine radiative forcing due to land surface changes (Chen et al. 2016a; Chen et al. 2016b; Chen et al. 2015; Hu et al. 2016; Hu et al. 2015; Li et al. 2015; Zhang and Liang 2014; Zhang and Liang 2018), and to evaluate environmental changes (Chen et al. 2017; He et al. 2014; He et al. 2013).

2.7 Land surface temperature (LST)

LST is a key parameter in many land processes. Thermal infrared (TIR) remote sensing provides direct observation of thermal emission from the land surface, enabling the estimation of LST under clear-sky conditions. Numerous algorithms have been proposed, but a long-term global high-resolution LST satellite product has yet to be found, especially for data collected prior to the year 2000.

The GLASS LST product was recently released (Zhou et al. 2019) and differs from most of the current satellite LST products. The GLASS LST product is based on a multi-algorithm ensemble approach, which combines nine split-window algorithms with the Bayesian Model Averaging (BMA) model. In the first phase, the GLASS LST product was produced for four discrete years with a spatial resolution of 0.05° for 1983 and 1993 and a spatial resolution of 1 km for 2003 and 2013. In the second phase, the product was expanded to cover 1981-2000 with a spatial resolution of 0.05°.

The GLASS LST products have been validated by in situ LST measurements. In the preliminary validation stage (Zhou et al. 2019), the AVHRR LST product had an RMSE of

313 2.89 K when validated with measurements from the Barrow site of the Baseline Surface
314 Radiation Network (BSRN) (Driemel et al. 2018). For the MODIS LST product, validation
315 with measurements from six grassland/cropland Surface Radiation Budget Network
316 (SURFRAD) sites indicated that the mean RMSE values are 1.82-2.15 K at night for
317 Terra/Aqua MODIS in 2003 and 2013. This accuracy is similar to that of the official MODIS
318 LST product. In the validation stage, the AVHRR LST product was validated with historical
319 in situ measurements from the SURFRAD data collected between 1995 and 2000, with a
320 mean bias error (MBE) of 0.21 K and a range of -1.59 – 2.71 K (site dependent), and a
321 standard deviation (STD) of 2.48 K with a range of 2.26 – 2.76 K (site dependent); and
322 water data from the National Data Buoy Center (NDBC) collected between 1981 and 2000
323 that has an MBE of 0.11 K with a range of -0.01 - 0.26 K and a STD of 0.80 K with a range
324 of 0.77 - 0.85 K.
325
326
327 A parallel effort has been undertaken to generate another GLASS AVHRR LST product
328 from 1981-2000 using a generalized split-window algorithm (Liu et al. 2019). The major
329 difference from the LST product described above is a further orbit drift correction that
330 normalizes the estimated LST to the same local time based on the diurnal temperature
331 cycle model and the Bayesian optimization algorithm. The validation results based on
332 measurements from six SURFRAD sites produced RMSEs from 2.2 to 4.1 K and MBEs from
333 -0.4 to 2.0 K.

2.8 Broadband emissivity

Surface thermal-infrared broadband emissivity (BBE) is a key variable for calculating the surface radiation budget, which is critical for addressing a variety of scientific and applied issues that are related to climate trends, weather prediction, hydrologic models, and biogeophysical models (Kustas et al. 2018; Liang et al. 2019; Wild et al. 2014). Jin and Liang (2006) demonstrated that incorporating a satellite-derived BBE product can significantly improve simulations with a coupled land surface and atmospheric model (National Center for Atmospheric Research Community Atmosphere Model + Community Land Model version 2).

The GLASS BBE products represent the broadband emissivity between 8 - 13.5 μm, which is the optimal spectral range for calculating longwave net radiation (Cheng et al. 2013). For the GLASS MODIS BBE product, land surfaces were classified into water, snow or ice, bare soil, vegetated surfaces, and transition zone, and their BBEs were calculated separately. The BBE of bare soil is estimated using the MODIS spectral reflective albedos (Cheng and Liang 2014), which are based on their linear relationship with the Advanced Spaceborne Thermal Emission and Reflection Radiometer (ASTER) spectral thermal emissivities that are converted to broadband emissivity. The vegetation BBE is calculated based on the leaf BBE, soil BBE, and LAI from a radiative transfer model (Cheng et al. 2016).

354 The GLASS AVHRR BBE product is generated from a similar algorithm, except that the
355 AVHRR surface visible and near-infrared reflectances were used to replace the MODIS
356 spectral albedos (Cheng and Liang 2013).
357
358 The GLASS BBE product was validated with field measurements of northern China from
359 2006 - 2011 (Dong et al. 2013). The differences over bare soils were within 0.02. The
360 differences between the GLASS BBE derived from the MODIS data and measurements
361 over fully vegetated surfaces were less than 0.005 (Cheng et al. 2016). Using ground
362 measurements collected from six sites in the desert regions of North America in 2008,
363 the mean BBE difference was 0.016 (Cheng and Liang 2014). Since no ground
364 measurements were available to validate the GLASS AVHRR BBE before 2000, we checked
365 the consistency between the 1 km MODIS BBE and the 0.05° AVHRR BBE products after
366 2000. The absolute value of mean difference and the RMSE were both less than 0.001.
367 We also compared the GLASS BBE with the North American ASTER Land Surface
368 Emissivity Database (Cheng et al. 2014) and found good agreement in both the summer
369 and winter seasons.
370
371
372 The GLASS BBE products have been used to estimate evaporation (Yang et al. 2020b) and
373 ET (Ma et al. 2019), compare with the retrievals of a new inversion algorithm as a
374 reference value (Ma et al. 2018), and to study climate impacts due to the widespread
375 deployment of utility-scale solar energy installations (Li et al. 2017).

2.9 Longwave downward and upward radiation

The surface radiation budget is dominated by longwave radiation at night and in polar regions for most of the year. To estimate instantaneous clear-sky longwave upwelling (LWUP) and downward (LWDN) radiation from the MODIS data, we developed a hybrid model for LWUP (Cheng and Liang 2016) and for LWDN (Cheng et al. 2017a). For cloudy-sky conditions, we estimated the LWDN using the single layer cloud model (Forman and Margulis 2009) with inputs from the MODIS cloud product. The cloudy-sky LWUP was calculated from the GLASS LST and BBE products.

For thermal radiation before 2000, we used the parameterization schemes to calculate clear-sky LWDN from reanalysis data (Cheng et al. 2019; Cheng et al. 2020; Guo et al. 2019) and used the GLASS LST and BBE products to calculate LWUP.

Validation of the clear-sky GLASS MODIS products used three ground measurements from six networks at 141 globally distributed sites and showed that the bias and RMSE were -3.77 Wm^{-2} and 26.94 Wm^{-2}, respectively, for LWDN, and -4.33 Wm^{-2} and 18.15 Wm^{-2}, respectively, for LWUP. The bias and RMSE of the calculated longwave net radiation (LWNT) were 0.70 Wm^{-2} and 26.7 Wm^{-2}, respectively, which are much better than those of other products (Zeng et al. 2020).

2.10 All-wave Net radiation

The all-wave surface net radiation (Rn) is the sum of the downward and upward fluxes of the shortwave (0.3 − 4 μm) and longwave (4 − 100 μm) spectra. The GLASS Rn product is produced based on its relationship with solar radiation and other meteorological information. After exploring linear regression models (Jiang et al. 2015) and multiple machine learning methods (Jiang et al. 2014), the MARS and random forest (RF) algorithms were selected to produce the GLASS daytime (Jiang et al. 2019) and daily Rn products. The DSR, normalized difference vegetation index (NDVI), and albedo from the GLASS products and meteorological values from the MERRA2 (Modern-Era Retrospective analysis for Research and Applications, Version 2) reanalysis data (Gelaro, et al., 2017) are the primary inputs.

The GLASS daytime and daily Rn products were validated with in situ measurements from more than 140 global sites. Comparisons were also made with CERES and two reanalysis products: the Japanese 55-year Reanalysis (JRA55) and the European Centre for Medium-Range Weather Forecasts (ECMWF) Reanalysis - Interim (ERA-Interim). The results in Table 2 show that the two satellite products (GLASS and CERES) are more accurate than the reanalysis datasets, and the GLASS Rn product exhibits the smallest RMSE and MBE on both daytime and daily scales.

We also calculated the average net radiation over land surfaces for the past decade. The GLASS net radiation product shows a similar temporal trend to the two reanalysis

products, while the CERES product has a trend of opposite sign due to changes in the versions of input data (Jia et al. 2018a).

2.11 Evapotranspiration (ET)

ET is a key variable linked to energy, water, and carbon exchange among the terrestrial biosphere, hydrosphere, and atmosphere. The GLASS ET product algorithm is based on the multi-model ensemble approach (Yao et al. 2014) and, in particular, the Bayesian model averaging (BMA) method, which merges five process-based ET estimates, such as the MODIS ET product algorithm (MOD16) (Mu et al. 2011), the revised remote sensing-based Penman-Monteith ET algorithm (RRS-PM) (Yuan et al. 2010), the Priestley-Taylor-based ET algorithm (PT-JPL) (Fisher et al. 2008), modified satellite-based Priestley-Taylor ET algorithm (MS-PT) (Yao et al. 2013), and the semi-empirical Penman ET algorithm of the University of Maryland (UMD-SEMI) (Wang et al. 2010).

The validation of the GLASS ET product used ground measurements from 240 eddy covariance flux tower sites and illustrated that the GLASS ET product using the BMA method enhances the latent heat flux (LE) estimates, with a smaller RMSE (35.3 Wm^{-2}) and a larger average R^2 (0.75) than the MODIS ET product (RMSE=45.3 Wm^{-2}, R^2=0.62) using the individual algorithms driven by the tower-specific and MERRA2 meteorological data. Additionally, Song et al. (2018a) compared five major satellite ET products over the Heihe river basin in China and found that the GLASS ET product was more accurate than the individual model calculations.

2.12 Gross primary production (GPP)

Vegetation GPP refers to the rate at which green plants in the ecosystem produce organic matter by assimilating carbon dioxide using solar energy through photosynthesis. The GLASS GPP algorithm originates from the Eddy Covariance – Light Use Efficiency (EC-LUE) model (Yuan et al. 2007). The original EC-LUE model is driven by only four variables: NDVI, PAR, air temperature, and the Bowen ratio of sensible to latent heat flux. The later version of the EC-LUE model substitutes the ratio of ET to net radiation for the Bowen ratio, and revises the RS-PM (Remote Sensing-Penman Monteith) model to quantify ET (Yuan et al. 2010). In order to accurately indicate the long-term changes in GPP, the GLASS GPP product uses the latest version of the EC-LUE model that integrates the impacts of several environmental variables: atmospheric CO2 concentrations, direct and diffuse radiation fluxes, and atmospheric water vapor pressure deficit (VPD) (Yuan et al. 2019).

The EC-LUE model has been validated throughout North America, Europe and East Asia using measurements from eddy covariance towers (Li et al. 2013; Yuan et al. 2014; Yuan et al. 2010; Yuan et al. 2007). The validations show that the EC-LUE model can successfully reproduce the spatial and temporal variabilities of GPP over various ecosystem types.

Several model comparisons also indicate the superior performance of the EC-LUE model over other LUE models. Previous studies compared the EC-LUE model and the MODIS GPP products based on measurements from eddy covariance towers in southeastern China and found that the EC-LUE model performed better than the MODIS algorithms (Xu

et al. 2013). A recent study compared eight satellite-based GPP models over various major grassland ecosystem types and found that the EC-LUE model had the best performance (Jia et al. 2018c). Evaluation at 85 eddy covariance towers, distributed globally, demonstrated that the GLASS GPP product is able to represent inter-annual variations and long-term trends because it integrates important environmental variables (Zheng et al. 2019).

The GLASS GPP product has been widely used to examine the spatial and temporal variations in GPP (Han et al. 2015; Hu et al. 2018; Ma et al. 2015; Wang et al. 2015; Xu et al. 2013). For example, Yuan et al. (2019) used the GLASS GPP product to investigate the impacts of atmospheric VPD on global terrestrial GPP and found persistent widespread decreases in GPP after the late 1990s due to increases in VPD, which offset the positive CO_2 fertilization effect. In addition, the GLASS GPP algorithm has been used to develop and improve other GPP models (Kanniah et al. 2009; Pasquato et al. 2015; Restrepo-Coupe et al. 2013; Verma et al. 2015).

3. Production and distributions

The GLASS product production system, which includes high-performance computing capabilities, is located at Beijing Normal University (Zhao et al. 2013). The system includes processing, management and data service modules and currently stores more than 3 PB of data.

The HDF-EOS file format is used to store the GLASS products. In addition, we use the JPG format to display product thumbnails and the XML format to store product metadata. All

of the products are provided in the sinusoidal map projection for the MODIS data at 500 m or 1 km spatial resolution, and in the geographic latitude/longitude map projection for the AVHRR data at a 0.05° spatial resolution. All products are also aggregated and distributed at 0.05° or coarser resolution.

The GLASS products can be downloaded from the following websites:

- http://www.glass.umd.edu
- http://www.geodata.cn/thematicView/GLASS.html

The first web site is in English, and the second one is mainly in Chinese.

4. Next Steps

We continue to improve the GLASS products in the following ways:

1) Enhancing the spatial resolutions of the current products. Several products (e.g., shortwave albedo, LAI and FVC) will ultimately have a spatial resolution of 250 m since 2000. A parallel project is being undertaken to generate some of these products, as well as new products, at a 30 m resolution, which are denoted as high-resolution GLASS (Hi-GLASS) products;

2) Improving the accuracy and quality of the current products by using advanced machine learning algorithms and more satellite data sources (e.g., European and Chinese satellite data);

3) Expanding the number of products. Efforts are being made to generate more land, atmospheric and oceanic climate data records (CDRs) from different satellite observations. Many algorithms for generating these products have been developed,

505 including those for top-of-atmosphere (TOA) shortwave albedo (Song et al. 2018b; Wang
506 and Liang 2016; Wang and Liang 2017), ocean shortwave albedo (Feng et al. 2016; Qu et
507 al. 2016) and longwave emissivity (Cheng et al. 2017b), land surface NDVI (Xiao et al.
508 2015a; Xiao et al. 2017b), fractional snow cover (Chen et al. 2018), surface air
509 temperature (Rao et al. 2020), and forest above-ground biomass (Yang et al. 2020a).
510 Some of these products correspond to ECVs and are available upon request;
511 4) Broadening dissemination of the GLASS products. In addition to giving more
512 presentations at conferences, workshops and summer schools, we are improving the
513 web user interface for effective and efficient data downloading and are distributing
514 GLASS product information to global users through the Global Earth Observation System
515 of Systems (GEOSS) data portal at https://www.geoportal.org/;
516 5) Fostering greater utilization of the GLASS products. We are developing collaborations
517 between the GLASS product team and other research projects and have planned the first
518 GLASS user conference for the summer of 2021.

Acknowledgements

This work was partially supported by the Chinese Grand Research Program on Climate Change and Response through grant 2016YFA0600103 and the National Earth System Science Data Center, China. Many colleagues and graduate students have contributed to the development of the GLASS products. We would like to thank the anonymous reviewers for their valuable comments and suggestions that have greatly improved the presentation of this paper.

References

Bao, Y., and Coauthors, 2014: Evaluation of CMIP5 earth system models in reproducing leaf area index and vegetation cover over the Tibetan Plateau. *J. Meteorol. Res.*, **28,** 1041-1060.

Baldocchi, D., and Coauthors, 2001: FLUXNET: A new tool to study the temporal and spatial variability of ecosystem-scale carbon dioxide, water vapor, and energy flux densities. *Bulletin of the American Meteorological Society*, **82,** 2415-2434.

Baret, F., and Coauthors, 2007: LAI, FAPAR and fCOVER CYCLOPES global products derived from VEGETATION. Part 1: principles of the algorithm. *Remote Sensing of Environment*, **113,** 275-286.

Cai, W., and Coauthors, 2014: Improved estimations of gross primary production using satellite-derived photosynthetically active radiation. *Journal of Geophysical Research: Biogeosciences*, **119,** 2013JG002456.

Camacho, F., J. Cemicharo, R. Lacaze, F. Baret, and M. Weiss, 2013: GEOV1: LAI, FAPAR essential climate variables and FCOVER global time series capitalizing over existing products. Part 2: Validation and intercomparison with reference products. *Remote Sensing of Environment*, **137,** 310-329.

Carter, C., and S. Liang, 2019: Evaluation of ten machine learning methods for estimating terrestrial evapotranspiration from remote sensing. *International Journal of Applied Earth Observation and Geoinformation*, **78,** 86-92.

Chen, X., S. Liang, and Y. Cao, 2016a: Satellite observed changes in the Northern Hemisphere snow cover phenology and the associated radiative forcing and feedback between 1982 and 2013. *Environ. Res. Lett.*, **11,** 084002.

Chen, X., S. Liang, and Y. Cao, 2017: Sensitivity of Summer Drying to Spring Snow-Albedo Feedback Throughout the Northern Hemisphere From Satellite Observations. *IEEE Geoscience and Remote Sensing Letters*, **14,** 2345-2349.

Chen, X., S. Liang, Y. Cao, and T. He, 2016b: Distribution, attribution, and radiative forcing of snow cover changes over China from 1982 to 2013. *Climatic Change*, **137,** 363-377.

Chen, X., S. Liang, Y. Cao, T. He, and D. Wang, 2015: Observed contrast changes in snow cover phenology in northern middle and high latitudes from 2001–2014. *Sci Rep*, **5,** 16820.

Chen, X., D. Long, S. Liang, L. He, C. Zeng, X. Hao, and Y. Hong, 2018: Developing a composite daily snow cover extent record over the Tibetan Plateau from 1981 to 2016 using multisource data. *Remote Sensing of Environment*, **215,** 284-299.

Cheng, J., and S. Liang, 2013: Estimating global land surface broadband thermal-infrared emissivity from the Advanced Very High Resolution Radiometer optical data. *Int. J. Digit. Earth***,** DOI: 10.1080/17538947.17532013.17783129.

Cheng, J., and S. Liang, 2014: Estimating the broadband longwave emissivity of global bare soil from the MODIS shortwave albedo product. *Journal of Geophysical Research: Atmospheres*, **119,** 614-634.

——, 2016: Global Estimates for High-Spatial-Resolution Clear-Sky Land Surface Upwelling Longwave Radiation From MODIS Data. *IEEE Transactions on Geoscience and Remote Sensing*, **54,** 4115-4129.

Cheng, J., S. Liang, and W. Wang, 2017a: Surface downward longwave radiation. *Comprehensive Remote Sensing Vol. 5 Earth's Energy Budget*, S. Liang, Ed., Elsevier, 196-216.

Cheng, J., F. Yang, and Y. Guo, 2019: A comparative study of bulk parameterization schemes for estimating cloudy-sky surface downward longwave radiation. *Remote Sensing*, **11,** 528.

Cheng, J., S. Liang, and J. Shi, 2020: Impact of Air Temperature Inversion on the Clear-Sky Surface Downward Longwave Radiation Estimation. *IEEE Transactions on Geoscience and Remote Sensing*.

Cheng, J., S. Liang, Y. Yao, and X. Zhang, 2013: Estimating the Optimal Broadband Emissivity Spectral Range for Calculating Surface Longwave Net Radiation. *IEEE Geoscience and Remote Sensing Letters*, **10,** 401-405.

Cheng, J., S. Liang, W. Verhoef, L. Shi, and Q. Liu, 2016: Estimating the Hemispherical Broadband Longwave Emissivity of Global Vegetated Surfaces Using a Radiative Transfer Model. *IEEE Transactions on Geoscience and Remote Sensing*, **54,** 905-917.

Cheng, J., S. Liang, Y. Yao, B. Ren, L. Shi, and H. Liu, 2014: A Comparative Study of Three Land Surface Broadband Emissivity Datasets from Satellite Data. *Remote Sensing*, **6,** 111-134.

Cheng, J., X. Cheng, S. Liang, R. Niclòs, A. Nie, and Q. Liu, 2017b: A Lookup Table-Based Method for Estimating Sea Surface Hemispherical Broadband Emissivity Values (8–13.5 μm). *Remote Sensing*, **9,** 245, doi:210.3390/rs9030245.

Dickinson, R. E., 1983: Land surface processes and climate-surface albedos and energy balance. *Advances in Geophysics*, **25,** 305-353.

Dong, L., J. Hu, S. Tang, and M. Min, 2013: Field Validation of GLASS Land Surface Broadband Emissivity (LSBE) Database using pseudo-invariant sand dune sites in North of China. *Int. J. Digit. Earth*, **,** DOI:10.1080/17538947.17532013.17822573.

Driemel, A., and Coauthors, 2018: Baseline Surface Radiation Network (BSRN): structure and data description (1992-2017). *Earth System Science Data*, **10,** 1491-1501.

Druel, A., and Coauthors, 2017: Towards a more detailed representation of high-latitude vegetation in the global land surface model ORCHIDEE (ORC-HL-VEGv1. 0). *Geosci. Model Dev.*, **10,** 4693.

598 Feng, Y., Q. Liu, Y. Qu, and S. Liang, 2016: Estimation of the Ocean Water Albedo From Remote
599 Sensing and Meteorological Reanalysis Data. *IEEE Transactions on Geoscience and Remote*
600 *Sensing*, **54,** 850-868.
601 Fensholt, R., I. Sandholt, and M. S. Rasmussen, 2004: Evaluation of MODIS LAI, fAPAR and the relation
602 between fAPAR and NDVI in a semi-arid environment using in situ measurements. *Remote*
603 *Sensing of Environment*, **91,** 490-507.
604 Fisher, J. B., K. P. Tu, and D. D. Baldocchi, 2008: Global estimates of the land-atmosphere water flux
605 based on monthly AVHRR and ISLSCP-II data, validated at 16 FLUXNET sites. *Remote Sensing of*
606 *Environment*, **112,** 901-919.
607 Forman, B., and S. Margulis, 2009: High-resolution satellite-based cloud-coupled estimates of total
608 downwelling surface radiation for hydrologic modelling applications. *Hydrology and Earth System*
609 *Sciences*, **13,** 969-986.
610 GCOS, 2016: The Global Observing System for Climate: Implementation Needs, GCOS-200, GOOS-214,
611 342 pp.
612 Gelaro, R., and Coauthors, 2017: The Modern-Era Retrospective Analysis for Research and
613 Applications, Version 2 (MERRA-2). *Journal of Climate*, **30,** 5419-5454.
614 Guimberteau, M., and Coauthors, 2018: ORCHIDEE-MICT (v8. 4.1), a land surface model for the high
615 latitudes: model description and validation. *Geosci. Model Dev.*, **11,** 121.
616 Guo, Y., J. Cheng, and S. Liang, 2019: Comprehensive assessment of parameterization methods for
617 estimating clear-sky surface downward longwave radiation. *Theoretical and Applied Climatology*,
618 1-14, https://doi.org/10.1007/s00704-00018-02423-00707.
619 Han, F., and Coauthors, 2015: Effects of climate change on phenology and primary productivity in the
620 desert steppe of Inner Mongolia. *J. Arid Land*, **7,** 251-263.
621 He, L., J. M. Chen, J. Pisek, C. B. Schaaf, and A. H. Strahler, 2012: Global clumping index map derived
622 from the MODIS BRDF product. *Remote Sensing of Environment*, **119,** 118-130.
623 He, T., S. Liang, and D.-X. Song, 2014: Analysis of global land surface albedo climatology and spatial-
624 temporal variation during 1981–2010 from multiple satellite products. *Journal of Geophysical*
625 *Research: Atmospheres*, **119,** 10,281-210,298.
626 He, T., S. Liang, Y. Yu, Q. Liu, and F. Gao, 2013: Greenland surface albedo changes 1981-2012 from
627 satellite observations. *Environ. Res. Lett.*, **8,** 044043, DOI:044010.041088/041748-
628 049326/044048/044044/044043.
629 Hu, L., W. Fan, H. Ren, S. Liu, Y. Cui, and P. Zhao, 2018: Spatiotemporal Dynamics in Vegetation GPP
630 over the Great Khingan Mountains Using GLASS Products from 1982 to 2015. *Remote Sensing*, **10,**
631 488.
632 Hu, Y., G. Jia, C. Pohl, X. Zhang, and J. van Genderen, 2016: Assessing surface albedo change and its
633 induced radiation budget under rapid urbanization with Landsat and GLASS data. *Theoretical and*
634 *applied climatology*, **123,** 711-722.
635 Hu, Y., M. Hou, G. Jia, X. Zhang, R. Xu, and Y. He, 2015: Comparison of three different methods to
636 identify fractional urban signals for improving climate modelling. *International Journal of Remote*
637 *Sensing*, **36,** 3274-3292.
638 Huang, H., C. Liu, X. Wang, G. S. Biging, Y. Chen, J. Yang, and P. Gong, 2017: Mapping vegetation
639 heights in China using slope correction ICESat data, SRTM, MODIS-derived and climate data.
640 *ISPRS Journal of Photogrammetry and Remote Sensing*, **129,** 189-199.
641 Huang, Y., S. Gerber, T. Huang, and J. W. Lichstein, 2016: Evaluating the drought response of CMIP5
642 models using global gross primary productivity, leaf area, precipitation, and soil moisture data.
643 *Global Biogeochemical Cycles*, **30,** 1827-1846.

644 Jia, A., S. Liang, B. Jiang, X. Zhang, and G. Wang, 2018a: Comprehensive Assessment of Global Surface
645 Net Radiation Products and Uncertainty Analysis. *Journal of Geophysical Research: Atmospheres*,
646 **123,** 1970-1989.
647 Jia, K., S. L. Liang, X. Q. Wei, Y. J. Yao, L. Q. Yang, X. T. Zhang, and D. Y. Liu, 2018b: Validation of Global
648 LAnd Surface Satellite (GLASS) fractional vegetation cover product from MODIS data in an
649 agricultural region. *Remote Sens. Lett.*, **9,** 847-856.
650 Jia, K., and Coauthors, 2016: Fractional vegetation cover estimation algorithm for Chinese GF-1 wide
651 field view data. *Remote Sensing of Environment*, **177,** 184-191.
652 Jia, K., and Coauthors, 2019: Long-Term Global Land Surface Satellite (GLASS) Fractional Vegetation
653 Cover Product Derived From MODIS and AVHRR Data. *IEEE J. Sel. Top. Appl. Earth Observ. Remote*
654 *Sens.*, **12,** 508-518.
655 Jia, K., and Coauthors, 2015: Global Land Surface Fractional Vegetation Cover Estimation Using
656 General Regression Neural Networks From MODIS Surface Reflectance. *Ieee Transactions on*
657 *Geoscience and Remote Sensing*, **53,** 4787-4796.
658 Jia, W., M. Liu, D. Wang, H. He, P. Shi, Y. Li, and Y. Wang, 2018c: Uncertainty in simulating regional
659 gross primary productivity from satellite-based models over northern China grassland. *Ecological*
660 *indicators*, **88,** 134-143.
661 Jiang, B., Y. Zhang, S. Liang, X. Zhang, and Z. Xiao, 2014: Surface Daytime Net Radiation Estimation
662 Using Artificial Neural Networks. *Remote Sensing*, **6,** 11031-11050.
663 Jiang, B., and Coauthors, 2019: Validation of the Surface Daytime Net Radiation Product From Version
664 4.0 GLASS Product Suite. *IEEE Geoscience and Remote Sensing Letters*, **16,** 509-513.
665 Jiang, B., and Coauthors, 2015: Empirical estimation of daytime net radiation from shortwave
666 radiation and ancillary information. *Agricultural and Forest Meteorology*, **211–212,** 23-36.
667 Jiapaer, G., S. Liang, Q. X. Yi, and J. P. Liu, 2015: Vegetation dynamics and responses to recent climate
668 change in Xinjiang using leaf area index as an indicator. *Ecological Indicators*, **58,** 64-76.
669 Jin, M., and S. Liang, 2006: Improve land surface emissivity parameter for land surface models using
670 global remote sensing observations. *Journal of Climate*, **19,** 2867-2881.
671 Kanniah, K. D., J. Beringer, L. B. Hutley, N. J. Tapper, and X. Zhu, 2009: Evaluation of Collections 4 and
672 5 of the MODIS Gross Primary Productivity product and algorithm improvement at a tropical
673 savanna site in northern Australia. *Remote Sensing of Environment*, **113,** 1808-1822.
674 Kustas, W. P., and Coauthors, 2018: The grape remote sensing atmospheric profile and
675 evapotranspiration experiment. *Bulletin of the American Meteorological Society*, **99,** 1791-1812.
676 Li, R. Q., Y. H. Gao, D. L. Chen, Y. X. Zhang, and S. S. Li, 2018a: Contrasting vegetation changes in dry
677 and humid regions of the Tibetan Plateau over recent decades. *Sci. Cold Arid Reg.*, **10,** 482-492.
678 Li, S., J. Weigand, and S. Ganguly, 2017: The Potential for Climate Impacts from Widespread
679 Deployment of Utility-Scale Solar Energy Installations: An Environmental Remote Sensing
680 Perspective. *J Remote Sensing & GIS*, **6,** 2.
681 Li, X., and Coauthors, 2013: Estimation of gross primary production over the terrestrial ecosystems in
682 China. *Ecol. Model.*, **261–262,** 80-92.
683 Li, X. L., H. Lu, L. Yu, and K. Yang, 2018b: Comparison of the Spatial Characteristics of Four Remotely
684 Sensed Leaf Area Index Products over China: Direct Validation and Relative Uncertainties. *Remote*
685 *Sensing*, **10,** 26.
686 Li, Y., M. Zhao, S. Motesharrei, Q. Mu, E. Kalnay, and S. Li, 2015: Local cooling and warming effects of
687 forests based on satellite observations. *Nat. Commun.*, **6,** 6603.
688 Liang, S., and J. Wang, 2019: *Advanced remote sensing: Terrestrial information extraction and*
689 *applications.* 2e ed. Academic Press/Elsevier, 985 pp.
690 Liang, S., D. Wang, T. He, and Y. Yu, 2019: Remote sensing of earth's energy budget: synthesis and
691 review. *Int. J. Digit. Earth*, **12,** 737-780.

692 Liang, S., T. Zheng, R. Liu, H. Fang, S. C. Tsay, and S. Running, 2006: Mapping incident
693 Photosynthetically Active Radiation (PAR) from MODIS Data. *Journal of Geophysical Research-*
694 *Atmospheres*, **111,** Art. No. D15208, doi:15210.11029/12005JD006730.
695 Liang, S., X. Zhang, Z. Xiao, J. Cheng, Q. Liu, and X. Zhao, 2013a: *Global LAnd Surface Satellite (GLASS)*
696 *products: Algorithms, validation and analysis.* Springer.
697 Liang, S., and Coauthors, 2013b: A Long-term Global LAnd Surface Satellite (GLASS) Dataset for
698 Environmental Studies. *Int. J. Digit. Earth*, **6,** 5-33.
699 Liu, N., Q. Liu, L. Wang, S. Liang, J. Wen, Y. Qu, and S. Liu, 2013a: A statistics-based temporal filter
700 algorithm to map spatiotemporally continuous shortwave albedo from MODIS data. *Hydrology*
701 *and Earth System Sciences*, **17,** 2121-2129, doi:2110.5194/hess-2117-2121-2013.
702 Liu, P., L. Hao, C. Pan, D. Zhou, Y. Liu, and G. Sun, 2017: Combined effects of climate and land
703 management on watershed vegetation dynamics in an arid environment. *Science of the Total*
704 *Environment*, **589,** 73-88.
705 Liu, Q., L. Wang, Y. Qu, N. Liu, S. Liu, H. Tang, and S. Liang, 2013b: Priminary Evaluation of the Long-
706 Term GLASS Albedo Product. *Int. J. Digit. Earth*, **6,** 69-
707 95,doi:10.1080/17538947.17532013.17804601.
708 Liu, W., and Coauthors, 2016: Hydrological recovery in two large forested watersheds of
709 southeastern China: the importance of watershed properties in determining hydrological
710 responses to reforestation. *Hydrology and Earth System Sciences*, **20,** 4747-4756.
711 Liu, X., B.-H. Tang, G. Yan, Z.-L. Li, and S. Liang, 2019: Retrieval of Global Orbit Drift Corrected Land
712 Surface Temperature from Long-term AVHRR Data. *Remote Sensing*, **11,** 2843.
713 Liu, Y. B., and Coauthors, 2018: Satellite-derived LAI products exhibit large discrepancies and can lead
714 to substantial uncertainty in simulated carbon and water fluxes. *Remote Sensing of Environment*,
715 **206,** 174-188.
716 Liu, Z., Q. Shao, and J. Liu, 2015: The performances of MODIS-GPP and-ET products in China and their
717 sensitivity to input data (FPAR/LAI). *Remote Sensing*, **7,** 135-152.
718 Ma, H., Q. Liu, S. Liang, and Z. Xiao, 2017a: Simultaneous Estimation of Leaf Area Index, Fraction of
719 Absorbed Photosynthetically Active Radiation and Surface Albedo from multiple-Satellite Data.
720 *IEEE Transactions on Geoscience and Remote Sensing*, **55,** 4334 - 4354,
721 doi:4310.1109/TGRS.2017.2691542.
722 Ma, H., S. Liang, Z. Xiao, and H. Shi, 2017b: Simultaneous inversion of multiple land surface
723 parameters from MODIS optical–thermal observations. *ISPRS Journal of Photogrammetry and*
724 *Remote Sensing*, **128,** 240-254.
725 Ma, H., S. Liang, Z. Xiao, and D. Wang, 2018: Simultaneous Estimation of Multiple Land Surface
726 Parameters from VIIRS Optical-Thermal data. *IEEE Geoscience and Remote Sensing Letters*, **15,**
727 151-160.
728 Ma, J., X. Yan, W. Dong, and J. Chou, 2015: Gross primary production of global forest ecosystems has
729 been overestimated. *Sci Rep*, **5,** 10820.
730 Ma, N., J. Szilagyi, Y. Zhang, and W. Liu, 2019: Complementary-relationship-based modeling of
731 terrestrial evapotranspiration across China during 1982–2012: Validations and spatiotemporal
732 analyses. *Journal of Geophysical Research: Atmospheres*, **124,** 4326-4351.
733 Ma, R., and Coauthors, 2017c: Assimilation of remotely-sensed leaf area index into a dynamic
734 vegetation model for gross primary productivity estimation. *Remote Sensing*, **9,** 188.
735 Meng, X., J. Cheng, and S. Liang, 2017: Estimating Land Surface Temperature from Feng Yun-
736 3C/MERSI Data Using a New Land Surface Emissivity Scheme. *Remote Sensing*, **9,** 1247.
737 Mu, Q., M. Zhao, and S. W. Running, 2011: Improvements to a MODIS global terrestrial
738 evapotranspiration algorithm. *Remote Sensing of Environment*, **115,** 1781-1800.

739 Mu, X., S. Huang, H. Ren, G. Yan, W. Song, and G. Ruan, 2015: Validating GEOV1 Fractional Vegetation
740 Cover Derived From Coarse-Resolution Remote Sensing Images Over Croplands. *IEEE J. Sel. Top.*
741 *Appl. Earth Observ. Remote Sens.*, **8,** 439-446.
742 Myneni, R. B., and Coauthors, 2002: Global products of vegetation leaf area and fraction absorbed
743 PAR from year one of MODIS data. *Remote Sensing of Environment*, **83,** 214-231.
744 NRC, 2004: *Climate Data Records from Environmental Satellites: Interim Report.* The National
745 Academies Press.
746 Pasquato, M., C. Medici, A. D. Friend, and F. Francés, 2015: Comparing two approaches for
747 parsimonious vegetation modelling in semiarid regions using satellite data. *Ecohydrology*, **8,**
748 1024-1036.
749 Peng, J., and Coauthors, 2015: Multi-scale validation strategy for satellite albedo products and its
750 uncertainty analysis. *Sci. China Earth Sci.*, **58,** 573-588.
751 Piao, S. L., and Coauthors, 2015: Detection and attribution of vegetation greening trend in China over
752 the last 30 years. *Global Change Biology*, **21,** 1601-1609.
753 Qu, Y., Q. Liu, S. Liang, L. Wang, N. Liu, and S. Liu, 2014: Improved direct-estimation algorithm for
754 mapping daily land-surface broadband albedo from MODIS data. *IEEE Transactions on Geoscience*
755 *and Remote Sensing*, **52,** 907-919.
756 Qu, Y., S. Liang, Q. Liu, X. Li, Y. Feng, and S. Liu, 2016: Estimating Arctic sea-ice shortwave albedo from
757 MODIS data. *Remote Sensing of Environment*, **186,** 32-46.
758 Rao, Y., and Coauthors, 2020: Estimating daily average surface air temperature using satellite land
759 surface temperature and top-of-atmosphere radiation products over the Tibetan Plateau.
760 *Remote Sensing of Environment*, **234,**
761 111462,https://doi.org/111410.111016/j.rse.112019.111462.
762 Restrepo-Coupe, N., and Coauthors, 2013: What drives the seasonality of photosynthesis across the
763 Amazon basin? A cross-site analysis of eddy flux tower measurements from the Brasil flux
764 network. *Agricultural and Forest Meteorology*, **182-183,** 128-144.
765 Shi, H., Z. Xiao, S. Liang, and X. Zhang, 2016: Consistent estimation of multiple parameters from
766 MODIS top of atmosphere reflectance data using a coupled soil-canopy-atmosphere radiative
767 transfer model. *Remote Sensing of Environment*, **184,** 40-57.
768 Shi, H., Z. Xiao, S. Liang, and H. Ma, 2017: A Method for Consistent Estimation of Multiple Land
769 Surface Parameters From MODIS Top-of-Atmosphere Time Series Data. *IEEE Transactions on*
770 *Geoscience and Remote Sensing*, **55,** 5158-5173.
771 Song, L., and Coauthors, 2018a: Monitoring and validating spatially and temporally continuous daily
772 evaporation and transpiration at river basin scale. *Remote Sensing of Environment*, **219,** 72-88.
773 Song, Z., S. Liang, D. Wang, Y. Zhou, and Y. Yu, 2018b: Long-term record of top-of-atmosphere albedo
774 generated from AVHRR data. *Remote Sensing of Environment*, **211,** 71-88.
775 Sun, Y., D. Wendi, D. E. Kim, and S.-Y. Liong, 2016: Development and application of an integrated
776 hydrological model for Singapore freshwater swamp forest. *Procedia engineering*, **154,** 1002-
777 1009.
778 Tang, H., K. Yu, O. Hagolle, K. Jiang, X. Geng, and Y. Zhao, 2013: A cloud detection method based on a
779 time series of MODIS surface reflectance images. *Int. J. Digit. Earth*, **6,** 157-171.
780 Tesemma, Z. K., Y. Wei, M. C. Peel, and A. W. Western, 2015: The effect of year-to-year variability of
781 leaf area index on Variable Infiltration Capacity model performance and simulation of runoff.
782 *Adv. Water Resour.*, **83,** 310-322.
783 Tian, X., and Coauthors, 2015: Simulation of forest evapotranspiration using time-series
784 parameterization of the Surface Energy Balance System (SEBS) over the Qilian Mountains.
785 *Remote sensing*, **7,** 15822-15843.

786 Tian, X., and Coauthors, 2017: Modeling forest above-ground biomass dynamics using multi-source
787 data and incorporated models: A case study over the qilian mountains. *Agricultural and forest*
788 *meteorology*, **246,** 1-14.
789 Verma, M., and Coauthors, 2015: Improving the performance of remote sensing models for capturing
790 intra- and inter-annual variations in daily GPP: An analysis using global FLUXNET tower data.
791 *Agricultural and Forest Meteorology*, **214-215,** 416-429.
792 Wang, D., and S. Liang, 2016: Estimating high-resolution top of atmosphere albedo from Moderate
793 Resolution Imaging Spectroradiometer data. *Remote Sensing of Environment*, **178,** 93-103.
794 Wang, D., and S. Liang, 2017: Estimating top-of-atmosphere daily reflected shortwave radiation flux
795 over land from MODIS data. *IEEE Transactions on Geoscience and Remote Sensing*, **55,** 4022 -
796 4031.
797 Wang, H., and Coauthors, 2018: Sensitivity of biogenic volatile organic compound emissions to leaf
798 area index and land cover in Beijing. *Atmospheric Chemistry and Physics*, **18,** 9583-9596.
799 Wang, J., J. Wang, H. Zhou, and Z. Xiao, 2017a: Detecting forest disturbance in northeast China from
800 GLASS LAI time series data using a dynamic model. *Remote Sensing*, **9,** 1293.
801 Wang, K. C., R. E. Dickinson, M. Wild, and S. Liang, 2010: Evidence for decadal variation in global
802 terrestrial evapotranspiration between 1982 and 2002: 1. Model development. *Journal of*
803 *Geophysical Research-Atmospheres*, **115,** D20112, DOI:20110.21029/22009jd013671.
804 Wang, L., H. Zhu, A. Lin, L. Zou, W. Qin, and Q. Du, 2017b: Evaluation of the latest MODIS GPP
805 products across multiple biomes using Global Eddy Covariance Flux Data. *Remote Sensing*, **9,** 418.
806 Wang, Q., H. Zheng, X. Zhu, and G. Yu, 2015: Primary estimation of Chinese terrestrial carbon
807 sequestration during 2001–2010. *Sci. Bull.*, **60,** 577-590.
808 Wang, R., J. M. Chen, Z. Liu, and A. Arain, 2017c: Evaluation of seasonal variations of remotely sensed
809 leaf area index over five evergreen coniferous forests. *ISPRS Journal of Photogrammetry and*
810 *Remote Sensing*, **130,** 187-201.
811 Wild, M., and Coauthors, 2014: The energy balance over land and oceans: an assessment based on
812 direct observations and CMIP5 climate models. *Climate Dynamics***,** 1-37.
813 Xiao, Z., S. Liang, and B. Jiang, 2017a: Evaluation of four long time-series global leaf area index
814 products. *Agricultural and Forest Meteorology*, **246,** 218-230.
815 Xiao, Z., S. Liang, and R. Sun, 2018: Evaluation of Three Long Time Series for Global Fraction of
816 Absorbed Photosynthetically Active Radiation (FAPAR) Products. *IEEE Transactions on Geoscience*
817 *and Remote Sensing*, **56,** 5509-5524.
818 Xiao, Z., S. Liang, T. Wang, and Q. Liu, 2015a: Reconstruction of Satellite-Retrieved Land-Surface
819 Reflectance Based on Temporally-Continuous Vegetation Indices. *Remote Sensing*, **7,** 9844-9864.
820 Xiao, Z., T. Wang, S. Liang, and R. Sun, 2016a: Estimating the Fractional Vegetation Cover from GLASS
821 Leaf Area Index Product. *Remote Sensing*, **8,** 337.
822 Xiao, Z., S. Liang, T. Wang, and B. Jiang, 2016b: Retrieval of Leaf Area Index (LAI) and Fraction of
823 Absorbed Photosynthetically Active Radiation (FAPAR) from VIIRS Time-Series Data. *Remote*
824 *Sensing*, **8,** 351.
825 Xiao, Z., S. Liang, R. Sun, J. Wang, and B. Jiang, 2015b: Estimating the fraction of absorbed
826 photosynthetically active radiation from the MODIS data based GLASS leaf area index product.
827 *Remote Sensing of Environment*, **171,** 105-117.
828 Xiao, Z., S. Liang, J. Wang, D. Xie, J. Song, and R. Fensholt, 2015c: A Framework for the Simultaneous
829 Estimation of Leaf Area Index, Fraction of Absorbed Photosynthetically Active Radiation and
830 Albedo from MODIS Time Series Data. *IEEE Transactions on Geoscience and Remote Sensing*, **53,**
831 3178-3197.

Xiao, Z., S. Liang, J. Wang, Y. Xiang, X. Zhao, and J. Song, 2016c: Long-time-series global land surface satellite leaf area index product derived from MODIS and AVHRR surface reflectance. *IEEE Transactions on Geoscience and Remote Sensing*, **54,** 5301-5318.

Xiao, Z., S. Liang, X. Tian, K. Jia, Y. Yao, and B. Jiang, 2017b: Reconstruction of Long-Term Temporally Continuous NDVI and Surface Reflectance From AVHRR Data. *IEEE J. Sel. Top. Appl. Earth Observ. Remote Sens.*, **10,** 5551-5568.

Xiao, Z. Q., S. Liang, J. D. Wang, P. Chen, X. J. Yin, L. Q. Zhang, and J. L. Song, 2014: Use of General Regression Neural Networks for Generating the GLASS Leaf Area Index Product From Time-Series MODIS Surface Reflectance. *Ieee Transactions on Geoscience and Remote Sensing*, **52,** 209-223.

Xu, B., and Coauthors, 2018: An integrated method for validating long-term leaf area index products using global networks of site-based measurements. *Remote Sensing of Environment*, **209,** 134-151.

Xu, X., and Coauthors, 2013: Implications of ice storm damages on the water and carbon cycle of bamboo forests in southeastern China. *Agricultural and forest meteorology*, **177,** 35-45.

Yang, L., S. Liang, and Y. Zhang, 2020a: A new method for generating a global forest aboveground biomass map from multiple high-level satellite products and ancillary information. *IEEE Journal in Special Topics in Applied Earth Observations and Remote Sensing***, 13,** 2587-2597.

Yang, L., K. Jia, S. Liang, J. Liu, and X. Wang, 2016: Comparison of Four Machine Learning Methods for Generating the GLASS Fractional Vegetation Cover Product from MODIS Data. *Remote Sensing*, **8,** 682.

Yang, W., Y. Wang, X. Liu, H. Zhao, R. Shao, and G. Wang, 2020b: Evaluation of the rescaled complementary principle in the estimation of evaporation on the Tibetan Plateau. *Science of The Total Environment*, **699,** 134367.

Yao, Y., and Coauthors, 2014: Bayesian multimodel estimation of global terrestrial latent heat flux from eddy covariance, meteorological, and satellite observations. *Journal of Geophysical Research: Atmospheres*, **119,** 2013JD020864.

Yao, Y. J., and Coauthors, 2013: MODIS-driven estimation of terrestrial latent heat flux in China based on a modified Priestley-Taylor algorithm. *Agricultural and Forest Meteorology*, **171,** 187-202.

Yu, T., R. Sun, Z. Q. Xiao, Q. Zhang, J. M. Wang, and G. Liu, 2018: Generation of High Resolution Vegetation Productivity from a Downscaling Method. *Remote Sensing*, **10,** 22.

Yuan, W., and Coauthors, 2014: Global comparison of light use efficiency models for simulating terrestrial vegetation gross primary production based on the LaThuile database. *Agricultural and forest meteorology*, **192,** 108-120.

Yuan, W., and Coauthors, 2019: Increased atmospheric vapor pressure deficit reduces global vegetation growth. *Sci. Adv.*, **5,** eaax1396.

Yuan, W. P., and Coauthors, 2010: Global estimates of evapotranspiration and gross primary production based on MODIS and global meteorology data. *Remote Sensing of Environment*, **114,** 1416-1431.

Yuan, W. P., and Coauthors, 2007: Deriving a light use efficiency model from eddy covariance flux data for predicting daily gross primary production across biomes. *Agricultural and Forest Meteorology*, **143,** 189-207.

Zeng, Q., J. Cheng, and L. Dong, 2020: Assessment of the long-term high-spatial resolution Global LAnd Surface Satellite (GLASS) surface longwave radiation product using ground measurements. *IEEE Journal in Special Topics in Applied Earth Observations and Remote Sensing***,** doi:10.1109/JSTARS.2020.2992472.

Zhang, X., S. Liang, G. Zhou, H. Wu, and X. Zhao, 2014: Generating Global LAnd Surface Satellite incident shortwave radiation and photosynthetically active radiation products from multiple satellite data. *Remote Sensing of Environment*, **152,** 318-332.

Zhang, X., and Coauthors, 2019: An Operational Approach for Generating the Global Land Surface Downward Shortwave Radiation Product from MODIS Data. *IEEE Transactions on Geoscience and Remote Sensing*, **57,** 4636-4650.

Zhang, Y., and S. Liang, 2014: Surface radiative forcing of forest disturbances over northeastern China *Environ. Res. Lett.*, **9,** 024002,doi:024010.021088/021748-029326/024009/024002/024002.

Zhang, Y., and S. Liang, 2018: Impacts of land cover transitions on surface temperature in China based on satellite observations. *Environ. Res. Lett.*, **13,** 024010.

Zhao, L., Z.-L. Yang, and T. J. Hoar, 2016: Global Soil Moisture Estimation by Assimilating AMSR-E Brightness Temperatures in a Coupled CLM4–RTM–DART System. *Journal of Hydrometeorology*, **17,** 2431-2454.

Zhao, X., and Coauthors, 2013: The Global Land Surface Satellite (GLASS) remote sensing data processing system and products. *Remote Sensing*, **5,** 2436-2450.

Zheng, Y., and Coauthors, 2019: Improved estimate of global gross primary production for reproducing its long-term variation, 1982-2017. *Earth System Science Data Discussion***,** https://doi.org/10.5194/essd-2019-5126.

Zhou, J., S. Liang, J. Cheng, Y. Wang, and J. Ma, 2019: The GLASS Land Surface Temperature Product. *IEEE Journal in Special Topics in Applied Earth Observations and Remote Sensing*, **12,** 10.1109/JSTARS.2018.2870130.

Zhu, H., A. Lin, L. Wang, Y. Xia, and L. Zou, 2016a: Evaluation of MODIS gross primary production across multiple biomes in China using eddy covariance flux data. *Remote Sensing*, **8,** 395.

Zhu, Z., and Coauthors, 2016b: Greening of the Earth and its drivers. *Nature Clim. Change*, **6,** 791-795.

Table Caption List:

Table 1 Characteristics of the GLASS products (Version 4). Products 1, 2, 7, 8, 9 and 11 correspond to the essential climate variables (ECV). Both shortwave net radiation, which can be calculated by products 2 and 5, and longwave net radiation, which can be calculated by products 3, 7 and 8, are also ECVs.

Table 2 Validation results of four daytime/daily Rn products against in-situ measurements (36,733 samples).

Figure Caption List:

Fig. 1. Validation of the V4 GLASS shortwave albedo product (6035 samples from the FLUXNET LaThuile Opened dataset).

Table 1 Characteristics of the GLASS products (Version 4). Products 1, 2, 7, 8, 9 and 11 correspond to the essential climate variables (ECV). Both shortwave net radiation, which can be calculated by products 2 and 5, and longwave net radiation, which can be calculated by products 3, 7 and 8, are also ECVs.

No.	Product	Temporal range	Temporal resolution	Spatial resolution
1	Leaf Area Index	1981-2018	8 days	0.05° from AVHRR 500m from MODIS
2	Broadband Albedo	1981-2018	8 days	0.05° from AVHRR 1km from MODIS
3	Broadband Emissivity	1981-2018	8 days	0.05° from AVHRR 1km from MODIS
4	Photosynthetically Active Radiation	2000-2018	daily	0.05°
5	Downward Shortwave Radiation	2000-2018	daytime/daily	0.05°
6	Downward Longwave Radiation	2000-2018	instantaneous	1km
7	All-wave Net Radiation	2000-2018	daily	0.05°
8	Land Surface Temperature	1981-2000	instantaneous	0.05°
9	Fraction of Absorbed Photosynthetically Active Radiation	1981-2018	8 days	0.05° from AVHRR 500m from MODIS
10	Fractional Vegetation Cover	1981-2018	8 days	0.05° from AVHRR 500m from MODIS
11	Evapotranspiration	1981-2018	8 days	0.05° from AVHRR 1km from MODIS
12	Gross Primary Production	1981-2018	8 days	0.05° from AVHRR 500m from MODIS

924

925 **Table 2 Validation results of four daytime/daily Rn products against in situ measurements**

	Daily (n=36,733)			Daytime (n=52,176)		
	R^2	RMSE ($W \cdot m^{-2}$)	MBE ($W \cdot m^{-2}$)	R^2	RMSE ($W \cdot m^{-2}$)	MBE ($W \cdot m^{-2}$)
GLASS	0.82	28.99	-2.73	0.80	52.93	5.56
CERES_SYN1deg Ed3A	0.72	36.01	3.53	0.82	55.25	23.92
JRA55	0.64	45.54	2.22	0.62	79.70	25.75
ERA-Interim	0.54	51.67	-5.96	0.64	74.18	20.86

926

927

928 **Fig. 1. Validation of the V4 GLASS shortwave albedo product using the FLUXNET LaThuile Opened**

929 **dataset (the color indicates the normalized density of the samples)**

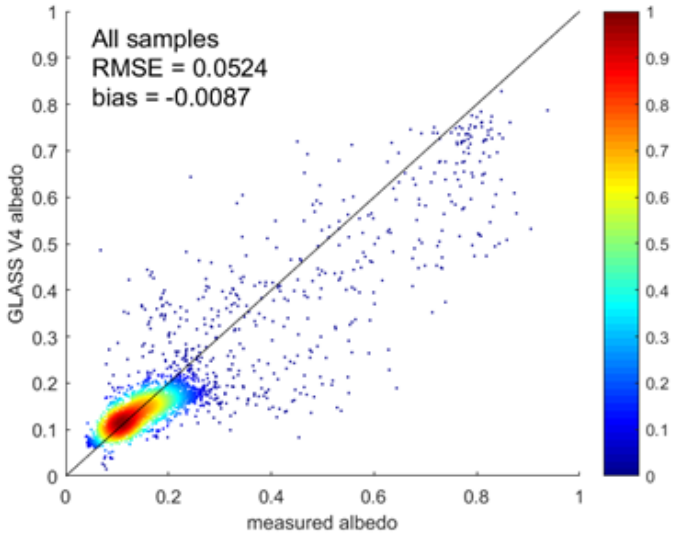

930

931

932